Nano Research
2022, 15(7): 6019–6025

ISSN 1998-0124 CN 11-5974/O4
https://doi.org/10.1007/s12274-022-4293-7

Atomic manganese coordinated to nitrogen and sulfur for oxygen evolution

Xue Bai[1,§], Liming Wang[3,4,§], Bing Nan[5,§], Tianmi Tang[1], Xiaodi Niu[2] (✉), and Jingqi Guan[1] (✉)

[1] Institute of Physical Chemistry, College of Chemistry, Jilin University, 2519 Jiefang Road, Changchun 130021, China
[2] College of Food Science and Engineering, Jilin University, Changchun 130062, China
[3] CAS Key Laboratory for Biomedical Effects of Nanomaterials and Nanosafety & CAS-HKU Joint Laboratory of Metallomics on Health and Environment, Institute of High Energy Physics, Chinese Academy of Sciences, Beijing 100049, China
[4] State Key Laboratory of Natural and Biomimetic Drugs, School of Pharmaceutical Sciences, Peking University, Beijing 100191, China
[5] Shanghai Synchrotron Radiation Facility, Shanghai Advanced Research Institute, Chinese Academy of Science, Shanghai 201210, China
[§] Xue Bai, Liming Wang, and Bing Nan contributed equally to this work.

Received: 25 January 2022 / **Revised:** 1 March 2022 / **Accepted:** 4 March 2022

ABSTRACT

Lack of high-efficiency, cost-efficient, and well-stocked oxygen evolution reaction (OER) electrocatalysts is a main challenge in large-scale implementation of electrolytic water. By regulating the electronic structure of isolated single-atom metal sites, high-performance transition-metal-based catalysts can be fabricated to greatly improve the OER performance. Herein, we demonstrate single-atom manganese coordinated to nitrogen and sulfur species in two-dimensional graphene nanosheets Mn-NSG (NSG means N- and S- codoped graphene) as an active and durable OER catalyst with a low overpotential of 296 mV in alkaline media, compared to that of the benchmark IrO_2 catalyst. Theoretical calculations and experimental measurements reveal that the Mn-N_3S sites in the graphene matrix are the most active sites for the OER due to modified electronic structure of the Mn site by three nitrogen and one sulfur atoms coordination, which show lower theoretical overpotential than the Mn-N_4 sites and over which the O–O formation step is the rate-determining step.

KEYWORDS

Mn-N-C, N/S co-coordination, oxygen evolution reaction, single-atom catalyst, theoretical calculations

1 Introduction

The electrochemical water splitting is an important approach for generating highly purified hydrogen by using renewable electricity, which involves hydrogen evolution reaction (HER) and oxygen evolution reaction (OER) [1–3]. Up to now, large-scale application of electrolytic water is still impeded by the lack of high-efficiency, cost-efficient, and well-stocked electrocatalysts to overcome the sluggish OER kinetics and improve the energy efficiency [4–6]. Although the OER energy barrier can be significantly reduced on RuO_2 and IrO_2 electrocatalysts, the scarcity heavily hinders their large-scale application in water splitting devices [7–9]. Therefore, development of high-performance transition-metal-based catalysts is the key to realize industrial application of electrolytic water [10–13].

Regulating the chemical component, geometric, and electronic structures of isolated single-atom metal sites is a feasible strategy to greatly improve the electrocatalytic performance. The natural oxygen-evolving center $CaMn_4O_5$ showed a very low overpotential and high turnover frequency (TOF, 100–400 s^{-1}) for water oxidation, suggesting that Mn is a highly active element for the OER [14]. However, manganese oxides needed large overpotentials (usually $\eta_{10} > 500$ mV) to achieve 10 $mA\cdot cm^{-2}$, indicating that there is a high energy barrier and the structure and coordination environment of Mn ions in the manganese oxides should not be optimal for the OER [15]. Downsizing Mn-based species to single atomic level and modulating the coordination configuration of Mn sites are efficient strategies to improve the catalytic performance [16–18]. We found that atomic manganese coordinated to four nitrogen atoms in the graphene exhibited a high TOF of 214 s^{-1} for chemical water oxidation and an η_{10} of 337 mV, indicating that the OER activity can be greatly enhanced by modulating the electronic structure of Mn sites [19]. Plenty of investigations showed that N-coordination is an effective strategy to adjust the d-band electron structure of transition metals and improve the electrocatalytic performance due to moderate electronegativity of N and its electron–donating effect [20–25]. Thereinto, M-N_4C_x (M = Mn, Fe, Co, Ni, Ru, Ir, etc.) configuration has been found to be efficient active structure for the OER [26–28]. Although great progress has been made on single-atom M-N-C catalysts for OER, the catalytic performance is still far from satisfactoriness [29]. To enhance the electrocatalytic OER performance, more efforts should be devoted to tune finely the spatial and electronic structures of active sites for further lowering the reaction energy barrier [30, 31]. Theoretical studies revealed that the electron–donating property of transition metal active sites can be modified by coordinating with proper nonmetallic atoms [32, 33], which favors lowering the energy barriers and improving the intrinsic electrocatalytic activity. Considering that

Address correspondence to Xiaodi Niu, niuxd@jlu.edu.cn; Jingqi Guan, guanjq@jlu.edu.cn

the electronegativity of S is between C and N, we forecasted that the partial substitution of N with S atoms in single-atom M-N-C catalysts can further adjust their electronic structures and thus promote the OER kinetics.

Herein, we report atomically dispersed Mn ions embedded into N- and S- co-doped graphene by one-pot pyrolysis of the mixture of $MnCl_2$, sulfur, and graphene oxide (GO) at 800 °C in an ammonia atmosphere. The obtained Mn-NSG ((NSG means N- and S- codoped graphene) nanosheets exhibit outstanding OER activity with a low η_{10} of 296 mV in alkaline media. Experiment and theory uncover that the superior OER activity is derived from the generation of atomic Mn coordinated to three N atoms and one S atom in the graphene matrix, which can greatly reduce the OER barrier and boost the reaction kinetics.

2 Experimental

2.1 Synthesis of Mn-NSG

Typically, 100 mg GO [34], 25 mg S power, and 2.5 mg $MnCl_2 \cdot 4H_2O$ (Mn/GO = 0.7 wt.%) were dispersed in water. Then, the mixture was poured into liquid nitrogen. After the water was dislodged by a freeze-drying equipment, the residuary yellow solid was annealed at 800 °C under NH_3 for 2 h to obtain black 0.7-Mn-NSG-800. For convenience, the 0.7-Mn-NSG-800 is simplified as Mn-NSG. Additionally, *c*-Mn-NSG-*T* (*c*: initial manganese content, *T*: annealing temperature) with different initial manganese content (0.3 wt.%–0.9 wt.%) and different annealing temperature (600–900 °C) was synthesized by a similar process.

For comparison, Mn-G and Mn-SG were prepared by annealing the precursors of $MnCl_2$/GO and $MnCl_2$/S/GO at 800 °C under N_2 for 2 h, respectively. Mn-NG was prepared by annealing the precursor of $MnCl_2$/GO at 800 °C under NH_3 for 2 h. Graphene (G) and NG were prepared by annealing GO at 800 °C under Ar and NH_3 for 2 h, respectively. SG was prepared by annealing the mixture of S/GO at 800 °C under N_2 for 2 h.

2.2 Characterization

X-ray diffraction (XRD) patterns were collected using a Shimadzu XRD-6000. High resolution transmission electron microscope (HRTEM) images were recorded on a JEM-2100 microscope. High-angle annular dark field-scanning transmission electron microscopy (HAADF-STEM) images were collected on a JEM-ARM 200F microscope. Scanning electron microscope (SEM) images were collected on a LEO 1530 VP microscope. X-ray photoelectron spectroscopy (XPS) was collected on a Thermo ESCALAB 250Xi. The X-ray absorption fine structure (XAFS) spectra of Mn-NSG at Mn K (E_0 = 6,539 eV) edge were performed at BL14W1 beamline of Shanghai Synchrotron Radiation Facility.

2.3 Computational methods

Density functional theory (DFT) calculations were carried out using the Vienna *ab initio* simulation package (VASP) [35, 36]. The Brillouin zone consisted of 2 × 2 × 2 Monkhorst–Pack points mesh. The graphene supercell with surface periodicity of 6 × 6 including 82 atoms was employed to construct the MnN_4-G, MnN_3S-G, and MnN_4S-G. The solvation effects were considered in VASP. The Gibbs free energies of OOH*, O*, and OH* on the electrode surface were evaluated by using the DFT calculations. The Gibbs free energy changes of reactions were calculated at the standard conditions.

3 Results and discussion

3.1 Materials characterization

The synthetic procedure of the Mn-NSG is depicted in Fig. 1(a). The structure of the Mn-NSG was analyzed by XRD. As exhibited in Fig. S1 in the Electronic Supplementary Material (ESM), no obvious peaks due to Mn/MnO_x nanoparticles can be found, indicating high dispersion of Mn-based species. The morphology

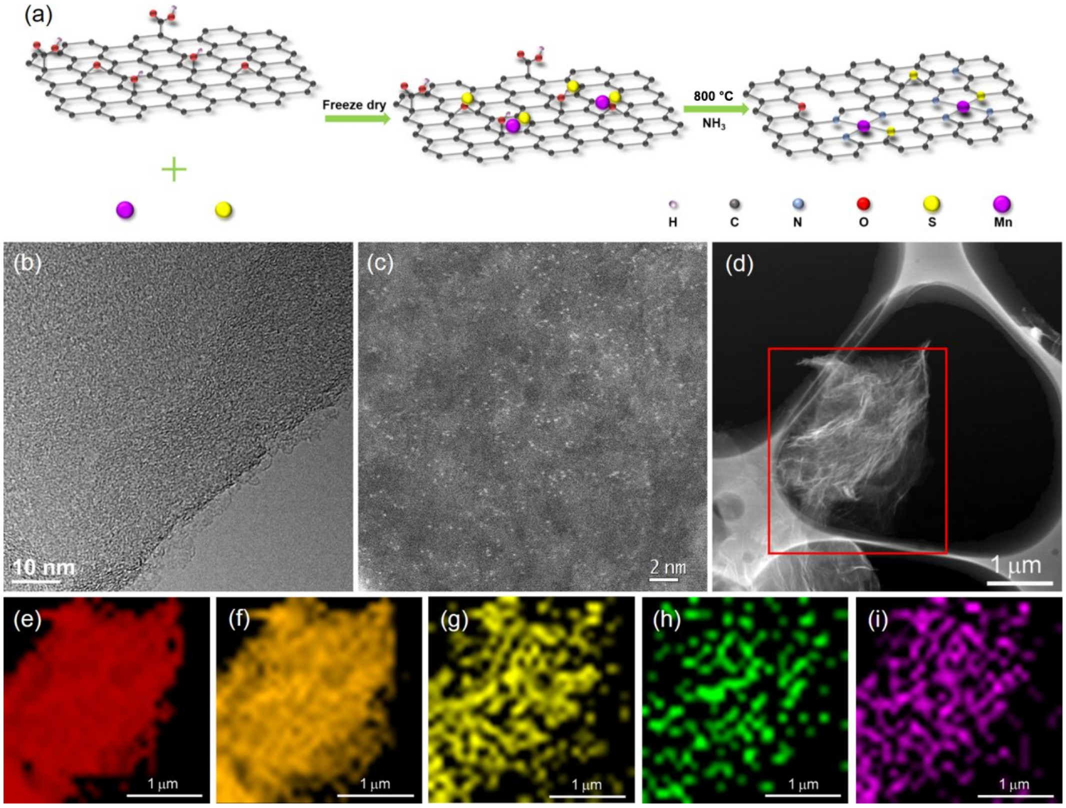

Figure 1 (a) Illustration for the synthetic process of Mn-NSG. (b) HRTEM image of Mn-NSG. (c) HAADF-STEM image of Mn-NSG. (d) STEM image and the corresponding EDS elemental mappings of (e) C, (f) N, (g) O, (h) S, and (i) Mn.

of the Mn-NSG was identified by SEM and TEM. As shown in Fig. S2 in the ESM, folded sheet-like structures are typically observed for the Mn-NSG and no Mn-based nanoparticles are observed on the Mn-NSG nanosheets by SEM or TEM, further implying highly dispersed manganese species. To uncover the existing state of the manganese species, we performed HRTEM and HAADF-STEM. As demonstrated in Fig. 1(b), no Mn-derived nanoparticles or nanoclusters can be found on the Mn-NSG nanosheets by HRTEM. The manganese species are atomically dispersed on the N/S-co-doped graphene nanosheets (Fig. 1(c)). The elemental mapping results further demonstrate that the manganese, nitrogen, and sulfur elements are well distributed on the Mn-NSG nanosheets (Figs. 1(d)–1(i)).

The surface compositions and manganese valence state were disclosed by XPS. As displayed in Fig. 2(a), the Mn-G is mainly consisted of C, O, and Mn elements, while the Mn-NG is primarily made up of C, O, N, and Mn elements. Moreover, the Mn-SG is principally composed by C, O, S, and Mn elements, while the Mn-NSG contains chiefly C, O, N, S, and Mn elements. The high-resolution Mn 2p spectrum of the Mn-NSG demonstrates the binding energies (BE) of the Mn $2p_{3/2}$ and Mn $2p_{1/2}$ peaks at 641.3 and 653.4 eV with two satellite peaks at 646.2 and 658.2 eV, respectively (Fig. 2(b)), which are characteristic of Mn^{2+} [19, 37]. Moreover, the BE of the Mn $2p_{3/2}$ peak for Mn-G, Mn-NG, Mn-SG, and Mn-NSG is different, which is centered at 641.5, 641.4, 641.7, and 641.3 eV, respectively, suggesting that the Mn ions in these samples should be in different coordination environments. The N 1s peak can be fitted into five types of nitrogen (Fig. 2(c)), which can be attributed to pyridinic N (398.4 eV), pyrrolic N (399.2 eV), Mn–N (400.2 eV), graphitic N (401.1 eV) and oxidized N (403.1) [33, 38, 39]. The high-resolution S 2p X-ray photoelectron spectroscopy (XPS) spectrum of Mn-NSG verifies the existence of Mn–S–C (163.5 eV), C–S (163.9 eV), and S–O (168.0 eV) bonds (Fig. 2(d)), indicating that Mn–S bonds are formed in the Mn-SG and Mn-SNG [40].

To further obtain the valence state and local coordination configurations of the Mn ions in Mn-NSG, XAFS was carried out (Fig. 3). The edge positions of Mn-NG and Mn-NSG are between Mn foil and Mn_3O_4, demonstrating the average valence state of Mn is between the two references (Fig. 3(a)). Additionally, the white-line position of Mn-NSG is slightly different from that of Mn-NG due to N/S co-coordination influencing the oxidation stat of Mn, agreeing well with the XPS analysis. The Fourier transform (FT) extended X-ray absorption fine structure (EXAFS) spectra of Mn-NSG and the references (Mn foil, Mn_3O_4, and Mn-NG) are demonstrated in Fig. 3(b), revealing that the coordination environment of Mn in Mn-NSG is quite different from that in Mn-NG. The mean bond length of Mn–N coordination in the Mn-NG is 1.88 ± 0.01 Å, close to the mean bond length (1.90 ± 0.01 Å) of Mn–N/S coordination in the Mn-NSG. The coordination number of Mn-N path is 2.5 ± 0.2. Moreover, the bond length of Mn–S coordination in the Mn-NSG is 2.50 ± 0.02 Å, and the coordination number is 1.7 ± 0.5 (Fig. 3(c) and Table S1 in the ESM). The EXAFS fitting spectrum shows that $Mn\text{-}N_3S_1$ structure could best reproduce the main features of the experimental curve of Mn-NSG (Fig. 3(d)).

3.2 OER performance

The OER activity of Mn-NSG was evaluated by electrochemical measurements in 1.0 M KOH. Figure 4(a) shows the linear sweep voltammetry (LSV) curves for Mn-G, Mn-NG, Mn-SG, and Mn-NSG. The IrO_2 was also included for comparison. The Mn-G displays inferior OER activity and the η_{10} is as high as 431 mV. The introduction of N or S elements results in obvious enhancement of catalytic activity. Mn-SG and Mn-NG require an η_{10} of 370 and 346 mV, respectively. Additionally, the OER activity can be further increased by N/S co-doping strategy and the Mn-NSG exhibits an η_{10} of 296 mV, much smaller than those of Mn-SG and Mn-NG, and close to that of IrO_2 (282 mV). The η_{10} value of Mn-NSG is superior or comparable to most of single-atom catalysts (Table S2 in the ESM), such as atomic Mn in NG (337 mV)[19], isolated $Fe\text{-}N_4$ moieties embedded onto porous carbon (430 mV) [41], hierarchical atomic Co catalyst (380 mV) [42], atomic Ni in NG (331 mV) [43], a Co-Fe double-atom catalyst (309 mV) [44], and atomic Ni-Fe sites immobilized into polymeric carbon nitride (310 mV) [45]. Optimizations of synthesis conditions show that the electrocatalytic OER performance of Mn-NSG is susceptive to annealing temperature

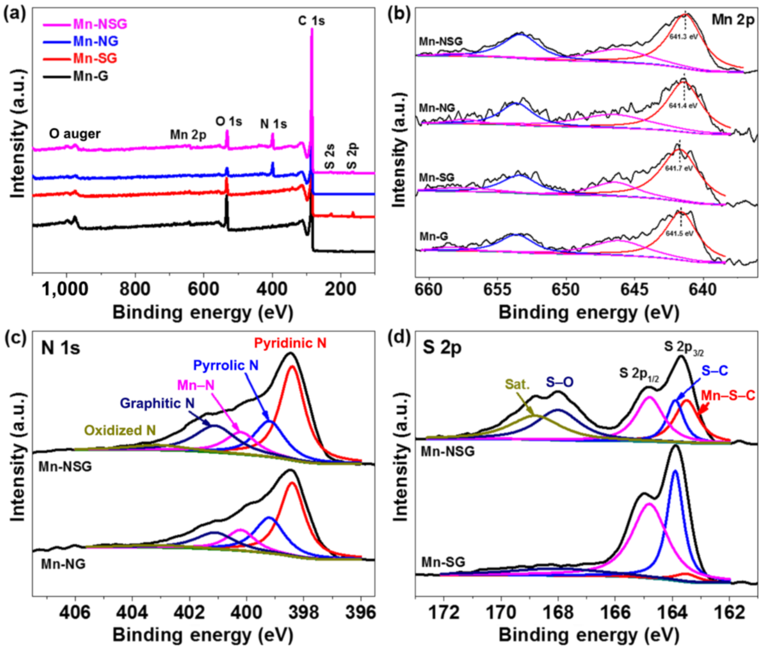

Figure 2 (a) XPS survey spectra of the Mn-G, Mn-SG, Mn-NG, and Mn-SNG. (b) Mn 2p XPS peaks of the Mn-G, Mn-SG, Mn-NG, and Mn-SNG. (c) N 1s XPS peaks of the Mn-NG and Mn-SNG. (d) S 2p XPS peaks of the Mn-SG and Mn-SNG. The black lines in Figs. 2(b)–2(d) are the experimental data, while the colored lines are the fitted data.

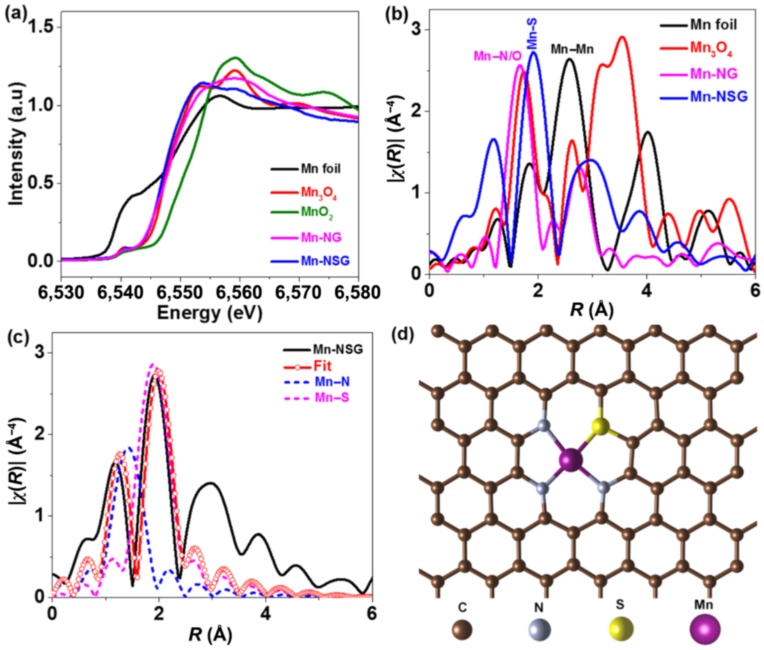

Figure 3 (a) Normalized XANES spectra at Mn K-edge of Mn foil, Mn_3O_4, MnO_2, Mn-NG, and Mn-NSG. (b) FT-EXAFS spectra, (c) FT-EXAFS fitting spectrum of Mn-NSG at the Mn K-edge, and (d) atomic model of MnN_3S-G.

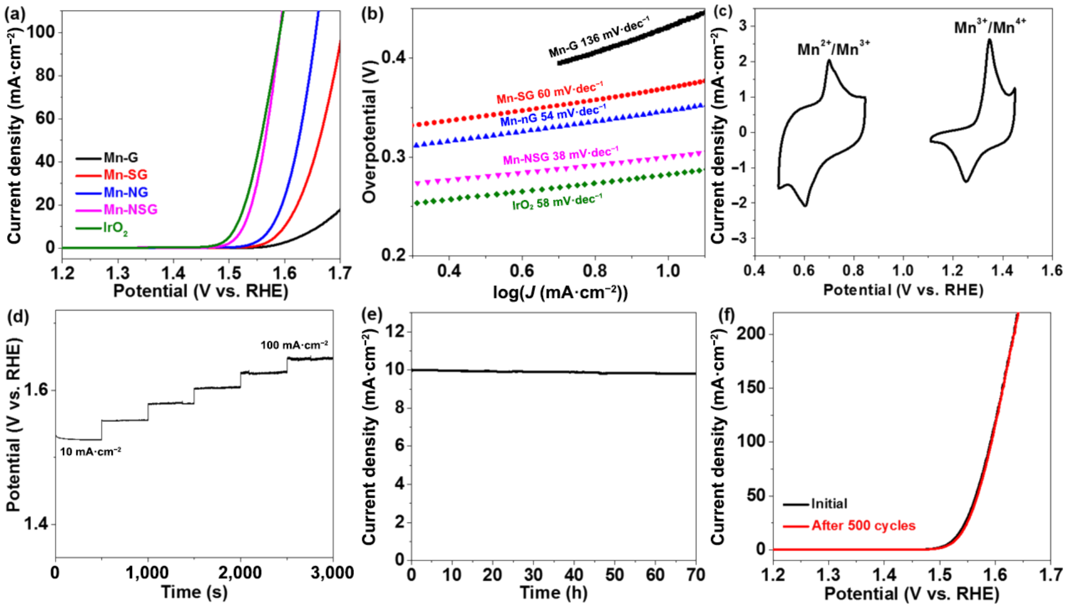

Figure 4 (a) LSV curves of commercial IrO_2, Mn-G, Mn-NG, Mn-SG, and Mn-NSG. (b) Tafel plots. (c) CVs of Mn-NSG. (d) Multi-current electrochemical process of Mn-NSG. (e) Plot of current density vs. time for Mn-NSG at 1.526 V. (f) Polarization curves of Mn-NSG before and after 500 cycles.

(Fig. S3 in the ESM) and Mn concentration (Fig. S4 in the ESM). The optimization results reveal that the Mn-NSG with initial 0.7 wt.% Mn content annealed at 800 °C exhibits the best OER performance. In addition to outstanding OER performance, Mn-NSG also exhibits excellent oxygen reduction reaction (ORR) activity in 0.1 M KOH (Fig. S5 and Table S3 in the ESM). Mn-NSG exhibits a half-wave potential of 0.85 V in 0.1 M KOH, more positive than Mn-G (0.719 V), Mn-SG (0.812 V), Mn-NG (0.817 V), and Pt/C (0.842 V).

The role of Mn in OER was investigated by comparing the electrocatalytic performance of Mn-free and Mn-doped samples. As displayed in Fig. S6 in the ESM, the graphene (G) shows an η_{10} of 490 mV, much higher than Mn-G. The OER activity can be significantly improved by N- or S-doping method and the NG and SG exhibit an η_{10} of 367 and 385 mV, respectively. However, NSG shows lower OER activity than NG and SG due to superfluous electron endowment effect [46]. Compared with Mn-doped counterparts, Mn-free NG, SG, and NSG all demonstrate higher overpotential, indicating that Mn is the efficient active site for OER.

The OER kinetics were analyzed by Tafel plots (Fig. 4(b)). The Tafel slope for Mn-NSG (38 mV·dec^{-1}) is much smaller than Mn-G (136 mV·dec^{-1}), Mn-NG (54 mV·dec^{-1}), and Mn-SG (60 mV·dec^{-1}), and even less than IrO_2 (58 mV·dec^{-1}), suggesting favorable OER kinetics on the Mn-NSG. The Tafel slope for Mn-NSG is near 40 mV·dec^{-1}, implying that the second electron transfer might be the rate-determining step [47]. Furthermore, compared with Mn-free counterparts, Mn-containing samples show lower Tafel slopes, indicating positive role of Mn in facilitating the OER kinetics. The electrochemically active surface area (ECSA) can reflect efficient active sites involved in the electrocatalytic reaction [48]. As illustrated in Figs. S7–S10 in the ESM, the ECSA for Mn-NSG is 250 cm^2, far larger than Mn-G (77 cm^2), Mn-NG (102 cm^2), and Mn-SG (84 cm^2), implying that

Mn-NSG possesses more active sites for OER than the latter. Furthermore, the electrochemical impedance spectra reveal that Mn-NSG shows a much smaller charge transfer resistance than Mn-G (Fig. S11 in the ESM), indicating more favorable OER kinetics in the former [33].

To probe the change of chemical valence states of Mn-based species during OER, cyclic voltammogram (CV) and differential pulse voltammetry (DPV) were carried out. As illustrated in Fig. 4(c), a reduction wave at $E_{1/2}$ = 0.65 V and an oxidation wave at $E_{1/2}$ = 1.30 V can be observed for the Mn-NSG, which is attributed to the sequentially occurring one-electron redox reactions concerning Mn^{3+}/Mn^{2+} and Mn^{4+}/Mn^{3+} couples, respectively. These consecutively occurring one-electron redox couples can be further verified by the DPV of Mn-NSG where two reduction peaks are evident in the range of 1.5 to 0.5 V and ascribed to the reductions of $Mn^{4+} \rightarrow Mn^{3+} \rightarrow Mn^{2+}$, respectively (Fig. S12 in the ESM). The structure of Mn sites can be reflected by the reduction peak position since Mn sites with different configurations possess different redox capacity. It can be seen from Fig. S12 in the ESM that the reduction peak positions due to Mn^{3+}/Mn^{2+} and Mn^{4+}/Mn^{3+} are quite different for Mn-G, Mn-NG, Mn-SG, and Mn-NSG, suggesting that the Mn ions in these samples are in different coordination environments. Specifically, the reduction peak position due to Mn^{4+}/Mn^{3+} for Mn-G, Mn-SG, Mn-NG, and Mn-NSG is centered at around 1.203, 1.192, 1.289, and 1.342 V, respectively. When Mn ions are coordinated with N atoms (i.e., Mn-NG), the reduction peak of Mn^{4+}/Mn^{3+} shifts more positively than those of Mn-G (Mn coordinated with O) and Mn-S (Mn coordinated with O/S), implying more difficulty of reduction of Mn^{4+} to Mn^{3+} due to electron–donating effect of N. When Mn ions are simultaneously coordinated with N and S, the reduction peak position is the most positive, implying that the electron–donating effect is more significant and the reduction of Mn^{4+} to Mn^{3+} is more difficult.

The OER durability of Mn-NSG was first evaluated by multi-current steps. For preparing high quality electrodes, the Mn-NSG was *in-situ* supported on a graphite plate by annealing $MnCl_2$/S/GO/graphite plate at 800 °C in NH_3 (Fig. 4(d)). At the beginning of 10 mA·cm^{-2}, the multi-step chronopotentiometric curve demonstrates that the potential quickly reaches a steady state at 1.526 V and holds steady for the rest of 500 s. The other steps also demonstrate similar tendencies up to 100 mA·cm^{-2}, reflecting excellent mass transport property and good stability of Mn-NSG. The OER stability of Mn-NSG was further assessed using a chronoamperometry technique. As exhibited in Fig. 4(e), no obvious current loss is observed after continuous operation for 70 h, indicating superior durability. In addition, the polarization curve of Mn-NSG exhibits no apparent current recession even after 500 cycles (Fig. 4(f)), suggesting outstanding electrocatalytic OER stability. The structure of Mn-NSG after OER test was analyzed by XRD (Fig. S13 in the ESM), which shows that the structure of the graphene substrate remains unchanged and no agglomeration of Mn-based species happens. The valence state of Mn in the Mn-NSG after OER test was detected by XPS (Fig. S14 in the ESM), demonstrating that the binding energy of Mn2p$_{3/2}$ is centered at around 642.5 eV, indicating that the Mn is oxidized to higher chemical valence of +4, which might be due to the absorption of oxygen-containing species on Mn sites [49].

3.3 OER mechanism

To probe the OER mechanism on the highly active Mn-NSG catalyst, DFT calculations were used to evaluate the OER energy barrier on the MnN_4-G, MnN_3S-G, and MnN_4S-G sites by using VASP. The optimized structures of MnN_xS-G configurations are shown in Figs. 5(a)–5(c), and the theoretical overpotential for all the models is used to evaluate the catalytic activities. As shown in Fig. 5(d), the theoretical overpotential of MnN_4-G (540 mV) is much higher than that of MnN_3S-G (490 mV). Based on previous work, S and C atoms neighboring the N atom in the N-S models are considered as typical electron donors, possessing high-

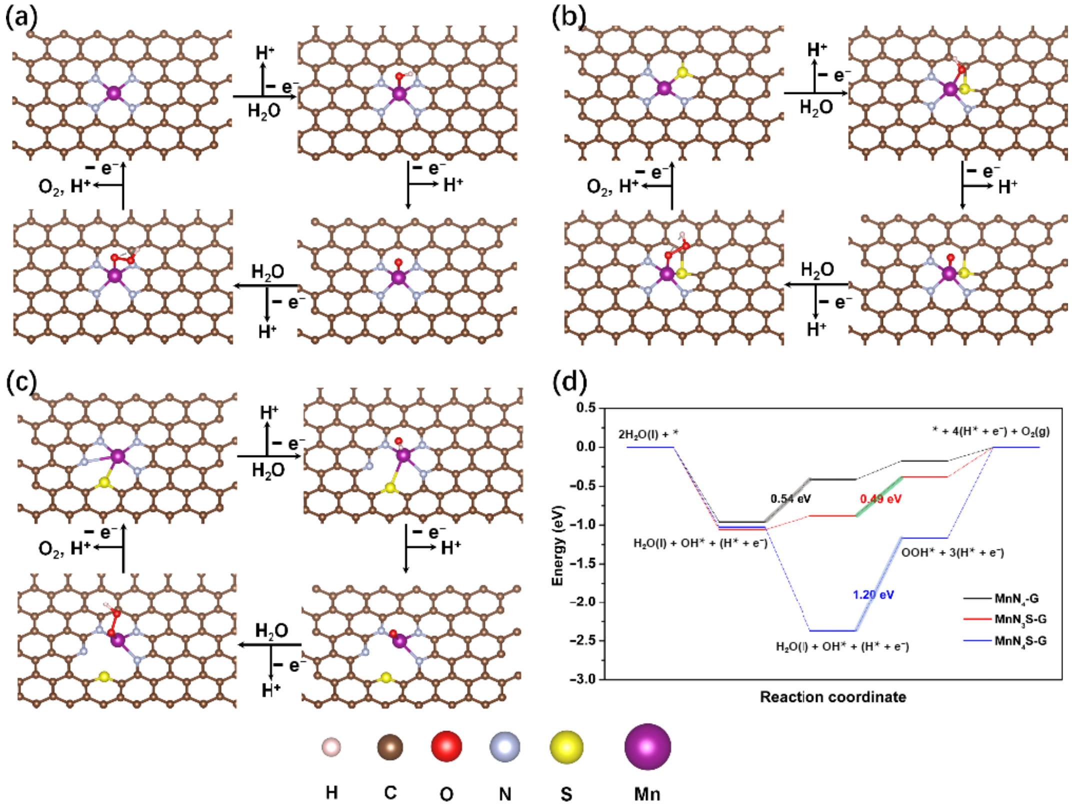

Figure 5 Top view of the initial structure and structures after adsorption of OH*, O*, and OOH* on (a) MnN_4-G, (b) MnN_3S-G, and (c) MnN_4S-G. (d) Free energy diagram for OER.

potential barriers for the rate-limiting step in OER [46]. Due to the intervention of S atom, the electron donation ability of Mn atom to its neighboring N atoms is deteriorated, which improves the OER catalytic performance [50]. Thus, the MnN_3S-G configuration is identified as the optimal catalytic structure. The difference of the overpotential between MnN_4-G and MnN_3S-G is mainly traceable in the formation of O^* intermediate. The rate-limiting step for MnN_4-G is the oxidation of OH^* to O^* species, while the O–O coupling step is the rate-limiting step for Mn-N_3S-G (Fig. 5(d)). To further investigate the catalytic mechanism, we also investigated the catalytic performance on MnN_4S-G. According to the calculations, the formation energy on MnN_4S-G is higher than those of MnN_4-G and MnN_3S-G, indicating that Mn-X_4 (four-coordinated models) can be more thermally stabilized than Mn-X_5 (five-coordinated models). Due to the excessive stabilization of O^* intermediate, MnN_4S-G exhibits the highest overpotential, as high as 1,200 mV (Fig. 5(d)). These results demonstrate that isolated single Mn site coupled with four atom coordination environments (e.g., three nitrogen and one sulfur) is favorable for achieving superior OER activity [19].

4 Conclusions

In conclusion, we put forward a one-pot annealing method to prepare an atomically dispersed Mn-based catalyst with N/S co-coordination, which exhibits superior OER performance with a low η_{10} of 296 mV, a Tafel slope of 38 mV·decade^{-1}, and outstanding stability in alkaline media, surpassing most transition metal-based single-atom catalysts. Experimental results and theoretical calculations uncover that one manganese ion coordinated to three nitrogen atoms and a sulfur atom in the graphene (MnN_3S-G) is the efficient active site for OER, on which Mn^{IV} is the key species and the O–O coupling step is the rate-determining step.

Acknowledgments

This work was supported by the National Natural Science Foundation of China (Nos. 22075099 and 31971322), the Education Department of Jilin Province (JJKH20220967KJ), the National Basic Research Program of China (Nos. 2016YFA0203200 and 2020YFA0710702), CAS President's International Fellowship Initiative (PIFI, 2021PM0059), and the State Key Laboratory of Natural and Biomimetic Drugs, Peking University.

Electronic Supplementary Material: Supplementary Material (XRD, SEM, XPS, and electrochemical measurements) is available in the online version of this article at https://doi.org/10.1007/s12274-022-4293-7.

References

[1] Zhang, H. B.; Cheng, W. R.; Luan, D. Y.; Lou, X. W. Atomically dispersed reactive centers for electrocatalytic CO_2 reduction and water splitting. *Angew. Chem. , Int. Ed.* **2021**, *60*, 13177–13196.

[2] Wang, Y. X.; Su, H. Y.; He, Y. H.; Li, L. G.; Zhu, S. Q.; Shen, H.; Xie, P. F.; Fu, X. B.; Zhou, G. Y.; Feng, C. et al. Advanced electrocatalysts with single-metal-atom active sites. *Chem. Rev.* **2020**, *120*, 12217–12314.

[3] Wang, Y.; Zheng, X. B.; Wang, D. S. Design concept for electrocatalysts. *Nano Res.* **2022**, *15*, 1730–1752.

[4] Wang, Y.; Huang, X.; Wei, Z. D. Recent developments in the use of single-atom catalysts for water splitting. *Chin. J. Catal.* **2021**, *42*, 1269–1286.

[5] Zhang, X. P.; Wang, H. Y.; Zheng, H. Q.; Zhang, W.; Cao, R. O–O bond formation mechanisms during the oxygen evolution reaction over synthetic molecular catalysts. *Chin. J. Catal.* **2021**, *42*, 1253–1268.

[6] Wang, Q. C.; Xue, X. X.; Lei, Y. P.; Wang, Y. C.; Feng, Y. X.; Xiong, X.; Wang, D. S.; Li, Y. D. Engineering of electronic states on Co_3O_4 ultrathin nanosheets by cation substitution and anion vacancies for oxygen evolution reaction. *Small* **2020**, *16*, 2001571.

[7] Gao, J. J.; Tao, H. B.; Liu, B. Progress of nonprecious-metal-based electrocatalysts for oxygen evolution in acidic media. *Adv. Mater.* **2021**, *33*, 2003786.

[8] Zhou, Y. N.; Li, J.; Gao, X. P.; Chu, W.; Gao, G. P.; Wang, L. W. Recent advances in single-atom electrocatalysts supported on two-dimensional materials for the oxygen evolution reaction. *J. Mater. Chem. A* **2021**, *9*, 9979–9999.

[9] Song, C. Y.; Liu, Y.; Wang, Y. C.; Tang, S. H.; Li, W. K.; Li, Q.; Zeng, J.; Chen, L.; Peng, H. C.; Lei, Y. P. Highly efficient oxygen evolution and stable water splitting by coupling NiFe LDH with metal phosphides. *Sci. China Mater.* **2021**, *64*, 1662–1670.

[10] Yao, D. X.; Gu, L. L.; Zuo, B.; Weng, S.; Deng, S. W.; Hao, W. J. A strategy for preparing high-efficiency and economical catalytic electrodes toward overall water splitting. *Nanoscale* **2021**, *13*, 10624–10648.

[11] Yu, M. Q.; Budiyanto, E.; Tüysüz, H. Principles of water electrolysis and recent progress in cobalt-, nickel-, and iron-based oxides for the oxygen evolution reaction. *Angew. Chem., Int. Ed.* **2022**, *61*, e202103824.

[12] Jing, H. Y.; Zhu, P.; Zheng, X. B.; Zhang, Z. D.; Wang, D. S.; Li, Y. D. Theory-oriented screening and discovery of advanced energy transformation materials in electrocatalysis. *Adv. Powder Mater.* **2022**, in press, https://doi.org/10.1016/j.apmate.2021.10.004.

[13] Chen, L.; Wang, Y. P.; Zhao, X.; Wang, Y. C/; Li, Q.; Wang, Q. C.; Tang, Y. G.; Lei, Y. P. Trimetallic oxyhydroxides as active sites for large-current-density alkaline oxygen evolution and overall water splitting. *J. Mater. Sci. Technol.* **2022**, *110*, 128–135.

[14] Najafpour, M. M.; Renger, G.; Hołyńska, M.; Moghaddam, A. N.; Aro, E. M.; Carpentier, R.; Nishihara, H.; Eaton-Rye, J. J.; Shen, J. R.; Allakhverdiev, S. I. Manganese compounds as water-oxidizing catalysts: From the natural water-oxidizing complex to nanosized manganese oxide structures. *Chem. Rev.* **2016**, *116*, 2886–2936.

[15] Jin, K.; Chu, A.; Park, J.; Jeong, D.; Jerng, S. E.; Sim, U.; Jeong, H. Y.; Lee, C. W.; Park, Y. S.; Yang, K. D. et al. Partially oxidized sub-10 nm MnO nanocrystals with high activity for water oxidation catalysis. *Sci. Rep.* **2015**, *5*, 10279.

[16] Li, J. Z.; Chen, M. J.; Cullen, D. A.; Hwang, S.; Wang, M. Y.; Li, B. Y.; Liu, K. X.; Karakalos, S.; Lucero, M.; Zhang, H. G. et al. Atomically dispersed manganese catalysts for oxygen reduction in proton-exchange membrane fuel cells. *Nat. Catal.* **2018**, *1*, 935–945.

[17] Han, X.; Zhang, T. Y.; Chen, W. X.; Dong, B.; Meng, G.; Zheng, L. R.; Yang, C.; Sun, X. M.; Zhuang, Z. B.; Wang, D. S. et al. Mn-N_4 oxygen reduction electrocatalyst: Operando investigation of active sites and high performance in zinc-air battery. *Adv. Energy Mater.* **2021**, *11*, 2002753.

[18] Guan, J. Q.; Bai, X.; Tang, T. M. Recent progress and prospect of carbon-free single-site catalysts for the hydrogen and oxygen evolution reactions. *Nano Res.* **2022**, *15*, 818–837.

[19] Guan, J. Q.; Duan, Z. Y.; Zhang, F. X.; Kelly, S. D.; Si, R.; Dupuis, M.; Huang, Q. G.; Chen, J. Q.; Tang, C. H.; Li, C. Water oxidation on a mononuclear manganese heterogeneous catalyst. *Nat. Catal.* **2018**, *1*, 870–877.

[20] Guan, J. Q. Effect of coordination surroundings of isolated metal sites on electrocatalytic performances. *J. Power Sources* **2021**, *506*, 230143.

[21] Huang, D. K.; Luo, Y. Z.; Li, S.; Liao, L.; Li, Y. X.; Chen, H.; Ye, J. H. Recent advances in tuning the electronic structures of atomically dispersed M-N-C materials for efficient gas-involving electrocatalysis. *Mater. Horiz.* **2020**, *7*, 970–986.

[22] Shi, Q. R.; Hwang, S.; Yang, H. P.; Ismail, F.; Su, D.; Higgins, D.; Wu, G. Supported and coordinated single metal site electrocatalysts. *Mater. Today* **2020**, *37*, 93–111.

[23] Li, X. Y.; Rong, H. P.; Zhang, J. T.; Wang, D. S.; Li, Y. D. Modulating the local coordination environment of single-atom

catalysts for enhanced catalytic performance. *Nano Res.* **2020**, *13*, 1842–1855.

[24] Yuan, C. Z.; Hui, K. S.; Yin, H.; Zhu, S. Q.; Zhang, J. T.; Wu, X. L.; Hong, X. T.; Zhou, W.; Fan, X.; Bin, F. et al. Regulating intrinsic electronic structures of transition-metal-based catalysts and the potential applications for electrocatalytic water splitting. *ACS Mater. Lett.* **2021**, *3*, 752–780.

[25] Chen, Y. J.; Gao, R.; Ji, S. F.; Li, H. J.; Tang, K.; Jiang, P.; Hu, H. B.; Zhang, Z. D.; Hao, H. G.; Qu, Q. Y. et al. Atomic-level modulation of electronic density at cobalt single-atom sites derived from metal-organic frameworks: Enhanced oxygen reduction performance. *Angew. Chem. , Int. Ed.* **2021**, *60*, 3212–3221.

[26] Zhang, Q. Q.; Guan, J. Q. Single-atom catalysts for electrocatalytic applications. *Adv. Funct. Mater.* **2020**, *30*, 2000768.

[27] Xu, H. X.; Cheng, D. J.; Cao, D. P.; Zeng, X. C. A universal principle for a rational design of single-atom electrocatalysts. *Nat. Catal.* **2018**, *1*, 339–348.

[28] Zhang, Q. Q.; Guan, J. Q. Applications of single-atom catalysts. *Nano Res.* **2022**, *15*, 38–70.

[29] Singh, B.; Sharma, V.; Gaikwad, R. P.; Fornasiero, P.; Zbořil, R.; Gawande, M. B. Single-atom catalysts: A sustainable pathway for the advanced catalytic applications. *Small* **2021**, *17*, 2006473.

[30] Wu, X.; Zhang, H. B.; Zuo, S. W.; Dong, J. C.; Li, Y.; Zhang, J.; Han, Y. Engineering the coordination sphere of isolated active sites to explore the intrinsic activity in single-atom catalysts. *Nano-Micro Lett.* **2021**, *13*, 136.

[31] Cui, T. T.; Wang, Y. P.; Ye, T.; Wu, J.; Chen, Z. Q.; Li, J.; Lei, Y. P.; Wang, D. S.; Li, Y. D. Engineering dual single-atom sites on 2D ultrathin N-doped carbon nanosheets attaining ultra-low-temperature zinc-air battery. *Angew. Chem., Int. Ed.*, in press, https://doi.org.10.1002/anie.202115219.

[32] Cabán-Acevedo, M.; Stone, M. L.; Schmidt, J. R.; Thomas, J. G.; Ding, Q.; Chang, H. C.; Tsai, M. L.; He, J. H.; Jin, S. Efficient hydrogen evolution catalysis using ternary pyrite-type cobalt phosphosulphide. *Nat. Mater.* **2015**, *14*, 1245–1251.

[33] Hou, Y.; Qiu, M.; Kim, M. G.; Liu, P.; Nam, G.; Zhang, T.; Zhuang, X. D.; Yang, B.; Cho, J.; Chen, M. W. et al. Atomically dispersed nickel-nitrogen-sulfur species anchored on porous carbon nanosheets for efficient water oxidation. *Nat. Commun.* **2019**, *10*, 1392.

[34] Hummers, W. S.; Offeman, R. E. Preparation of graphitic oxide. *J. Am. Chem. Soc.* **1958**, *80*, 1339–1339.

[35] Kresse, G.; Hafner, J. *Ab initio* molecular dynamics for liquid metals. *Phys. Rev. B Condens. Matter* **1993**, *47*, 558–561.

[36] Kresse, G.; Hafner, J. *Ab initio* molecular-dynamics simulation of the liquid-metal-amorphous-semiconductor transition in germanium. *Phys. Rev. B Condens. Matter* **1994**, *49*, 14251–14269.

[37] Kaneti, Y. V.; Guo, Y. N.; Septiani, N. L. W.; Iqbal, M.; Jiang, X. C.; Takei, T.; Yuliarto, B.; Alothman, Z. A.; Golberg, D.; Yamauchi, Y. Self-templated fabrication of hierarchical hollow manganese-cobalt phosphide yolk–shell spheres for enhanced oxygen evolution reaction. *Chem. Eng. J.* **2021**, *405*, 126580.

[38] Chen, M. J.; Li, X.; Yang, F.; Li, B. Y.; Stracensky, T.; Karakalos, S.; Mukerjee, S.; Jia, Q. Y.; Su, D.; Wang, G. F. et al. Atomically dispersed MnN_4 catalysts via environmentally benign aqueous synthesis for oxygen reduction: Mechanistic understanding of activity and stability improvements. *ACS Catal.* **2020**, *10*, 10523–10534.

[39] Shang, H. S.; Jiang, Z. L.; Zhou, D. N.; Pei, J. J.; Wang, Y.; Dong, J. C.; Zheng, X. S.; Zhang, J. T.; Chen, W. X. Engineering a metal-organic framework derived Mn-N_4-C_xS_y atomic interface for highly efficient oxygen reduction reaction. *Chem. Sci.* **2020**, *11*, 5994–5999.

[40] Choi, C. H.; Kim, M.; Kwon, H. C.; Cho, S. J.; Yun, S.; Kim, H. T.; Mayrhofer, K. J. J.; Kim, H.; Choi, M. Tuning selectivity of electrochemical reactions by atomically dispersed platinum catalyst. *Nat. Commun.* **2016**, *7*, 10922.

[41] Pan, Y.; Liu, S. J.; Sun, K. A.; Chen, X.; Wang, B.; Wu, K. L.; Cao, X.; Cheong, W. C.; Shen, R. A.; Han, A. J. et al. A bimetallic Zn/Fe polyphthalocyanine-derived single-atom Fe-N_4 catalytic site: A superior trifunctional catalyst for overall water splitting and Zn-air batteries. *Angew. Chem. , Int. Ed.* **2018**, *57*, 8614–8618.

[42] Sun, X. P.; Sun, S. X.; Gu, S. Q.; Liang, Z. F.; Zhang, J. X.; Yang, Y. Q.; Deng, Z.; Wei, P.; Peng, J.; Xu, Y. et al. High-performance single atom bifunctional oxygen catalysts derived from ZIF-67 superstructures. *Nano Energy* **2019**, *61*, 245–250.

[43] Fei, H. L.; Dong, J. C.; Feng, Y. X.; Allen, C. S.; Wan, C. Z.; Volosskiy, B.; Li, M. F.; Zhao, Z. P.; Wang, Y. L.; Sun, H. T. et al. General synthesis and definitive structural identification of MN_4C_4 single-atom catalysts with tunable electrocatalytic activities. *Nat. Catal.* **2018**, *1*, 63–72.

[44] Bai, L. C.; Hsu, C. S.; Alexander, D. T. L.; Chen, H. M.; Hu, X. L. A cobalt-iron double-atom catalyst for the oxygen evolution reaction. *J. Am. Chem. Soc.* **2019**, *141*, 14190–14199.

[45] Wu, C. C.; Zhang, X. M.; Xia, Z. X.; Shu, M.; Li, H. Q.; Xu, X. L.; Si, R.; Rykov, A. I.; Wang, J. H.; Yu, S. S. et al. Insight into the role of Ni-Fe dual sites in the oxygen evolution reaction based on atomically metal-doped polymeric carbon nitride. *J. Mater. Chem. A* **2019**, *7*, 14001–14010.

[46] Zhao, Z. H.; Li, M. T.; Zhang, L. P.; Dai, L. M.; Xia, Z. H. Design principles for heteroatom-doped carbon nanomaterials as highly efficient catalysts for fuel cells and metal-air batteries. *Adv. Mater.* **2015**, *27*, 6834–6840.

[47] Burke, M. S.; Kast, M. G.; Trotochaud, L.; Smith, A. M.; Boettcher, S. W. Cobalt-iron (oxy)hydroxide oxygen evolution electrocatalysts: The role of structure and composition on activity, stability, and mechanism. *J. Am. Chem. Soc.* **2015**, *137*, 3638–3648.

[48] Fei, H. L.; Dong, J. C.; Arellano-Jiménez, M. J.; Ye, G. L.; Dong Kim, N.; Samuel, E. L. G.; Peng, Z. W.; Zhu, Z.; Qin, F.; Bao, J. M. et al. Atomic cobalt on nitrogen-doped graphene for hydrogen generation. *Nat. Commun.* **2015**, *6*, 8668.

[49] Sun, Y. M.; Hu, X. L.; Luo, W.; Xia, F. F.; Huang, Y. H. Reconstruction of conformal nanoscale MnO on graphene as a high-capacity and long-life anode material for lithium ion batteries. *Adv. Funct. Mater.* **2013**, *23*, 2436–2444.

[50] Shinde, S. S.; Lee, C. H.; Sami, A.; Kim, D. H.; Lee, S. U.; Lee, J. H. Scalable 3D carbon nitride sponge as an efficient metal-free bifunctional oxygen electrocatalyst for rechargeable Zn-air batteries. *ACS Nano* **2017**, *11*, 347–357.